



Obtaining sols, gels and mesoporous nanopowders of hydrothermal nanosilica

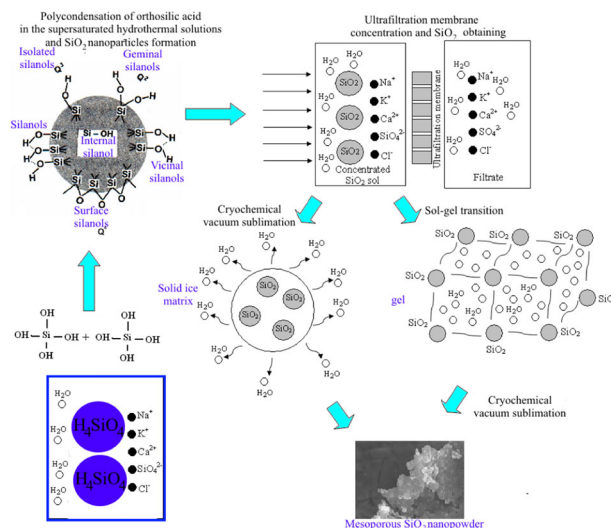
Vadim Potapov¹ · Roman Fediuk² · Denis Gorev¹

Received: 4 November 2019 / Accepted: 3 January 2020 / Published online: 13 January 2020
© Springer Science+Business Media, LLC, part of Springer Nature 2020

Abstract

Experiments were performed to obtain SiO₂ sols, gels, and mesoporous nanopowders based on hydrothermal medium. To achieve this, polycondensation of orthosilicic acid (OSA) at certain pH and temperature, as well as ultrafiltration membrane concentration, sol–gel transition, and cryochemical vacuum sublimation were done. The dynamic light scattering, scanning and tunneling electron microscopy, low-temperature nitrogen adsorption, and others methods determined the physical and chemical characteristics of nanosized SiO₂ samples. By choosing the pore size of the ultrafiltration membranes at the sol concentration stage, one can control the ratio of the SiO₂ content to the total salt content and provide a zeta potential of nanoparticles sufficient for the stability of the sols. It was shown that by varying the temperature at the polycondensation stage from 20 to 90 °C at pH = 8.5–9.3, it is possible to control the final average diameter of SiO₂ particles in the range from 5 to 100 nm, respectively. The specific surface area of particles are 50–500 m²/g, the average diameter of the mesoporous powders in the range of 2–15 nm; the fraction of the area (<4%) and volume (<0.25%) of micropores are low.

Graphical Abstract



✉ Roman Fediuk
roman44@yandex.ru

¹ Research Geotechnological Center, Far Eastern Branch of Russian Academy of Sciences, 30, Severo-Vostochny Highway, Petropavlovsk-Kamchatsky 683002, Russian Federation

² School of Engineering, Far Eastern Federal University, 8, Sukhanova Str., Vladivostok 690950, Russian Federation

Keywords Hydrothermal solution · Kinetics of orthosilicic acid polycondensation · Ultrafiltration membranes, Cryochemical vacuum sublimation · SiO₂ sols, Gels · Nanopowders

Highlights

- Three forms of nanosilica produced from hydrothermal solution: liquid sols, gels, and solid powders.
- Kinetic of orthosilicic acid regulated by temperature; diameters of silica particles are 5–100 nm.
- By membrane pores, we separate silica nanoparticles from water molecules and ions of dissolved salts.
- Specific surface areas of silica nanopowders can achieve 500 m²/g.

1 Introduction

Currently, there is a high growth rate of industrial consumption of various types of amorphous silica. In high-tech industries, the use of SiO₂ in nanodispersed form—sols, gels and powders—is expanding. Due to the high specific surface area (up to 1000 m²/g) and chemical activity, SiO₂ nanoparticles are used to create materials with improved or new properties. There are known applications of nano-SiO₂ for the production of ceramics, glass, precision casting molds, catalyst supports, sorbents, rubber fillers, polymeric materials, paper, thin coatings—nanofilms, fluorescent plates, as well as in the construction industry, medicine, and agriculture. Accordingly, it is relevant to search for new sources and technologies for producing nanosized SiO₂ with low cost.

The sol–gel process is a developed method for producing solid materials based on molecular forms of a substance [1, 2]. At the first stage of the process, hydrolysis and polycondensation of molecules and the production of sols of colloidal particles are used as precursors for the final products, in a large number of cases based on metal alkoxides and chlorides. The precursor for SiO₂ is tetraethoxysilane and alkali metal silicates (Na, K, Li). The sol–gel process uses sol–gel transition, catalysis, coagulation and precipitation, centrifugation, drying to remove the solvent, ultrasonic cavitation to break the polymer chains, and reduce the molecular weight, etc. The structure and morphology of the final solid phase can be in a wide range from individual unbound colloidal particles to extended chain networks of polymers [3, 4]. Under certain conditions, colloidal particles of sols can reach significant sizes, while precipitating and forming crystal-like matrices of noble opal [5]. If the interaction forces between the particles are strong enough, then they can form bound polymer chains before they reach significant size. In this case, polymer chains are precipitated by aggregation or flocculation, forming a low-density polymer matrix, suitable for the formation of glass, and ceramic components of high performance in two-dimensional and three-dimensional form [6]. With a suitable sol viscosity, glass and ceramic fiber can be isolated for optical sensors and heat insulators. A wide range of ceramic powders can be obtained by sol deposition. When creating

nanomaterials, the great importance is attached to the monodisperse distribution of particles to achieve a high degree of ordering in colloidal crystals and polycrystalline solid colloids resulting from aggregation [7–9].

The use of materials obtained by the sol–gel method is widely known—these are protective coatings, including those using spraying, electrophoresis, injection [10, 11]; thin coatings and fibers [12]; nanopowders; optical elements [13, 14]; medical preparations [15]. SiO₂ is one of the most common components for producing nanopowders, thin films, fibers, nanotubes, nanowires, monodispersed spheres with a solid core and mesoporous coating, additives to hard films to increase tensile strength, hardness of hybrid coatings, porous composite ceramics, SiO₂–Me_xO_y nanocomposites, etc. [16–32]. The possibility of obtaining colloidal SiO₂ based on cheap waste of glass powder was shown in [33].

From the point of view of sol–gel process, hydrothermal media are a new precursor for the production of SiO₂ sols, gels, nanopowders. For the full development of this resource requires the development of a technological route taking into account the parameters of the hydrothermal medium:

- (1) Temperature, pH, ion concentration, ionic strength of the hydrothermal medium;
- (2) kinetics of the formation of SiO₂ nanoparticles as a result of polycondensation of orthosilicic acid (OSA);
- (3) sizes, concentration, morphology of SiO₂ nanoparticles;
- (4) stability of SiO₂ nanoparticles in an aqueous medium, etc.

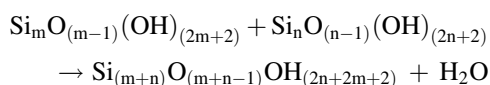
The purpose of the article is to determine the parameters of the processes necessary to obtain nanodispersed forms of SiO₂ on the basis of a hydrothermal medium: SiO₂ sols, gels, and mesoporous nanopowders with controlled characteristics.

2 Materials and preparation

2.1 Characteristics of the hydrothermal solution

To obtain nanosized forms of SiO₂, hydrothermal medium of the Mutnovsky deposit (south of Kamchatka, Russia) was

used, which contain SiO₂ due to the dissolution of the aluminosilicate minerals of the earth's crust (orthoclase, microcline K(AlSi₃O₈), albite Na(AlSi₃O₈), anorthite Ca(Al₂Si₂O₈), and others). In hydrothermal medium under conditions of elevated pressures (15–25 MPa) and temperatures (250–300 °C and higher), molecules of OSA are formed. After the solution reaches the surface, pressure and temperature decrease, the hydrothermal medium becomes supersaturated with respect to the solubility of amorphous silica and hydrolysis and polycondensation of OSA molecules take place in it, leading to the formation of spherical SiO₂ nanoparticles with diameters from 5–100 to 300–600 nm:



In addition to silica in the initial solution are other components, the concentrations of which are shown in Table 1.

The amount of silicon that entered the solution during chemical interaction with the rocks can be estimated from the solubility of C_{qu} (mol/kg) of α -quartz in pure water at absolute temperature T (K) [34]:

$$\lg C_{qu} = -1.468 + 252.9/T - 3.217 \times 10^5/T^2 \quad (1)$$

In a supersaturated hydrothermal medium, the solubility of amorphous silica C_e (mol/kg) versus absolute temperature T was evaluated using the following equation [35]:

$$\lg C_e = -0.1185 - 1.126 \times 10^3/T \\ + 2.3305 \times 10^5/T^2 - 3.6784 \times 10^7/T^3 \quad (2)$$

Polyatomic aggregates resulting from polycondensation acquire a three-dimensional structure in the form of colloidal silica particles. After completion of the polycondensation, part

Table 1 Characteristics of the hydrothermal solution from the Mutnovsky geothermal electric power plant productive wells

Component	mg/l	mg/eq. l	Component	mg/l	mg/eq. l
Na ⁺	239.4	10.413	Cl ⁻	198.5	5.591
K ⁺	42.0	1.074	HCO ₃ ⁻	81.0	1.327
Ca ²⁺	1.6	0.0798	CO ₃ ²⁻	19.9	0.663
Mg ²⁺	0.72	0.0592	SO ₄ ²⁻	192.1	3.9995
Fe ^{2,3+}	<0.1	<0.0053	HS ⁻	4.95	0.15
Al ³⁺	0.27	0.033	H ₂ S ⁰	5.92	–
NH ₄ ⁺	1.1	0.0609	F ⁻	n.d.	n.d.
Li ⁺	0.71	0.102	Anion amount	496.5	11.73
Cation amount	285.9	11.827	H ₃ BO ₃	106.9	–
pH	9.35	–	(H ₄ SiO ₄) _t	1190	–
			(H ₄ SiO ₄) _s	222.0	–
			Mineralization	1638.9	–

ionic strength of the solution $I_s = 14.218$ mmol/kg, electrical conductivity $\sigma_{el} = 1.1–1.3$ mS/cm, n.d.—the concentration was not determined, (–)—the values were not calculated

of the silicon continues to remain in the form of molecules of OSA H₄SiO₄, the concentration of C_s of which is close to the solubility of amorphous silica $C_e(T)$ in equilibrium with colloidal silica. In addition to colloidal particles and silicic acid molecules, a small amount of silicic acid ions (H₃SiO₄⁻, H₂SiO₄²⁻, HSiO₃⁻, etc.) and polysilicon acid macromolecules are present in the solution. As follows from the results obtained in [36], at a temperature of 20–180 °C and pH = 7.0–9.2, the proportion of dimers with respect to OSA, whose concentration is close to the solubility of $C_e(T)$, does not exceed 1.0%, the proportion of trimers is 0.1%, tetramers and low molecular weight cyclic polymers (up to 6 units of SiO₂) <0.1%. The fraction of H₃SiO₄⁻ and H₂SiO₄²⁻ ions under these conditions does not exceed 14.0%. The sum of the concentrations of colloidal silica C_{col} , soluble silicic acid C_s and silicic acid ions C_{in} is the total content of silica in the solution C_t :

$$C_t = C_{col} + C_s + C_{in} \quad (3)$$

2.2 Preparation of sols, gels, and nanopowders

The final particle sizes of silica depend primarily on the temperature and pH at which the polycondensation of the OSA molecules takes place. An increase in the polycondensation temperature and a decrease in pH slow down the reaction and increase the final particle size. At the polycondensation stage, the temperature ranged from 20 to 90 °C (precooling in heat exchangers), pH from 9.2 to 4.0 (solution acidification). The range of silica concentrations in the initial solution is $C_t = 400–800$ mg/kg (the sum of the concentrations of the colloidal phase and dissolved silica).

Concentrated silica sols were obtained from the liquid phase of hydrothermal solutions after OSA polycondensation by a three-step ultrafiltration membrane concentration: at the first step—the SiO₂ content in sol was increased from 0.05 to 0.3–0.4 wt%, at the 2nd step—up to 10 wt%, on the 3rd—up to 20–30 wt% and higher. The capillary type ultrafiltration membrane cartridge had an inner diameter of capillaries of 0.8 mm, a filtering surface area of 55 m², and a minimum mass weight cut off parameter MWCO = 10–100 kD.

Gel samples were obtained from concentrated sols by acidification and lowering the pH from 8–9 to 5–6.

SiO₂ nanopowders were obtained by cryochemical vacuum sublimation of sols and gels. Before sublimation in a vacuum chamber, the sols and silica gels were dispersed using a nozzle, the droplets were solidified in liquid nitrogen at a temperature of 77 K, and cryogranules were obtained. After dispersion, the droplet size was 30–100 μ m, the corresponding average droplet cooling rate was about 125 K/s, and the crystallization rate was 0.26 mm/s. The small size of the sol droplets, as well as the high heat transfer surface made it possible to achieve a quick hardening of the droplets, and the absence of particle

coagulation. The particle sizes in the powders did not exceed the particle sizes in the sols. Vacuum sublimation took place at pressures of 0.02–0.05 mmHg without fragments of droplet moisture and particles sticking together. To accelerate sublimation, the heating was used. The temperature range of the heating surfaces in different parts of the vacuum chamber as it was heated during sublimation was from -80 to $+25$ °C.

2.3 Methods of investigations

To study the characteristics of sols and powders, modern methods were used: dynamic light scattering and electrophoretic light scattering (Zetasizer, Malvern, UK), scanning electron microscopy (SEM), transmission electron microscopy (TEM), scanning transmission electron microscopy in a high-angle annual dark field (STEM HAADF), scanning transmission electron microscopy in a bright field (STEM BF) (JEM-100CX, JEOL, Japan), low-temperature nitrogen adsorption (ASAP-2010, Micromeritics, USA), X-ray diffraction analysis (ARL X'TRA, Thermo Scientific, Switzerland). To determine the concentration of impurity components in nanopowders, a S4 PIONEER X-ray fluorescence spectrometer (Bruker, GmbH, Germany) was used.

The dependences of the shear stress τ and the dynamic viscosity η of sols and gels on the strain rate G_p were measured under shear strain using a RheoStress rheometer (Haake, GmbH, Germany) in the mode of oscillating (dynamic) strains in the range rotation frequencies of plate G_p from 0.1 to 1000.0 Hz with varying shear stress amplitude from 0.01 to 10,000.0 Pa.

Sol's density was measured by areometers. To measure pour density of noncompacted silica nanopowders Scott's volumeter PT-SV100 with inclined shelves to pour powder's samples in tested volume was used.

The OSA and total silica contents in hydrothermal solutions and concentrated sols were measured by the yellow molybdate colorimetric method of Iler [37].

The total dissolved salts (TDS, mg/dm³) of sols as well as electrical conductivity were measured with an I-500 ionometric transducer.

3 Kinetics of polycondensation of orthosilicic acid in a hydrothermal medium

The nucleation rate of silicic acid in an aqueous solution (nucl/(kg s)) is described by the equation [38, 39]:

$$I_N = Q_{LP} \cdot Z \cdot R_{MD} \cdot A_{cr} \cdot N_A \cdot M_{Si}^{-1} \cdot e^{-\Delta F_{cr}/k_B \cdot T} \quad (4)$$

where $Q_{LP} = 3.34 \cdot 10^{25} \text{ kg}^{-1}$ the Lohse-Pound factor; k_B —the Boltzmann constant;

M_{Si} —the molar mass of SiO₂; N_A —the Avogadro number; T —the absolute temperature, K;

$A_{cr} = 4 \cdot \pi \cdot R_c^2$ —critical nucleus surface area, m²;

$\Delta F_{cr} = \sigma_{sw} \cdot A_{cr} / 3 = (16 \cdot \pi / 3) \cdot \sigma_{sw}^3 (M_{Si} / \rho \cdot N_A \cdot k_B \cdot T \cdot \ln S_m)^2$ —change in free energy associated with the formation of a nucleus of critical radius R_c ; ρ —density of amorphous silica, kg/m³;

σ_{sw} —surface tension at the silica–water interface, J/m²;

Z —Zeldovich factor.

$$Z = \sqrt{\frac{\partial^2 \Delta F_{cr} / \partial n_{cr}^2}{2 \cdot \pi \cdot k_B \cdot T}} \quad (5)$$

where $n_{cr} = (4 \cdot \pi / 3) \cdot (\rho \cdot N_A / M_{Si}) \cdot R_c^3$ —number of SiO₂ molecules in the nucleus of critical size;

$R_c = 2 \cdot \sigma_{sw} \cdot M_{Si} / (\rho \cdot N_A \cdot k_B \cdot T \cdot \ln S_m)$ critical radius; R_{MD} —the rate of molecular deposition of silicic acid (g cm² min⁻¹), which determines the particle growth rate:

$$R_{MD} = F(pH, pH_{nom}) \cdot k_{OH}(T) \cdot f_f(S_a) \cdot (1 - S_N^{-1}) \quad (6)$$

where $k_{OH}(T)$, $F(pH, pH_{nom})$, $f_f(S_a)$ —auxiliary functions depending on temperature, pH, ionic strength I_s , and supersaturation S_m .

3.1 Kinetics of polycondensation at 20 °C

Table 2 lists the results of determining the concentration of silicic acid C_s depending on the polymerization duration t , as well as the supersaturation $S_m = C_s(t) / C_e(20 \text{ °C})$ of the solution. Figure 1a shows the experimental dependence of the supersaturation $S_m = C_s(t) / C_e$ on the polymerization duration t_p obtained in the first series of measurements at $C_e = 160.7 \text{ mg/kg}$. The characteristic polycondensation time, at which the value of supersaturation decreased $e = 2.71$ times from the initial one, was $\tau_p = 1.98, h = 118.8 \text{ min}$.

3.2 Kinetics of polycondensation at 50 °C

The experiments on the kinetics of polycondensation were performed at 50 °C (Fig. 1b). For experiments, a sample of the solution was heated to 100 °C and maintained at this temperature for a time sufficient to dissolve colloidal silica.

Table 2 The dependence of the concentration of silicic acid on the duration of polymerization in a hydrothermal solution at a temperature of 20 °C, $C_i = 411.25 \text{ mg/kg}$, pH = 8.47, $C_e = 160.7 \text{ mg/kg}$

t_p, h	$C_s, \text{ mg/kg}$	$S_m, \text{ mg/kg}$	t_p, h	$C_s, \text{ mg/kg}$	$S_m, \text{ mg/kg}$
0.0	390.6	2.43	4.0	190.6	1.18
1.0	300.0	1.86	5.0	183.1	1.13
2.0	234.4	1.45	24.0	167.5	1.0
3.0	201.9	1.25	48.0	137.5	1.0

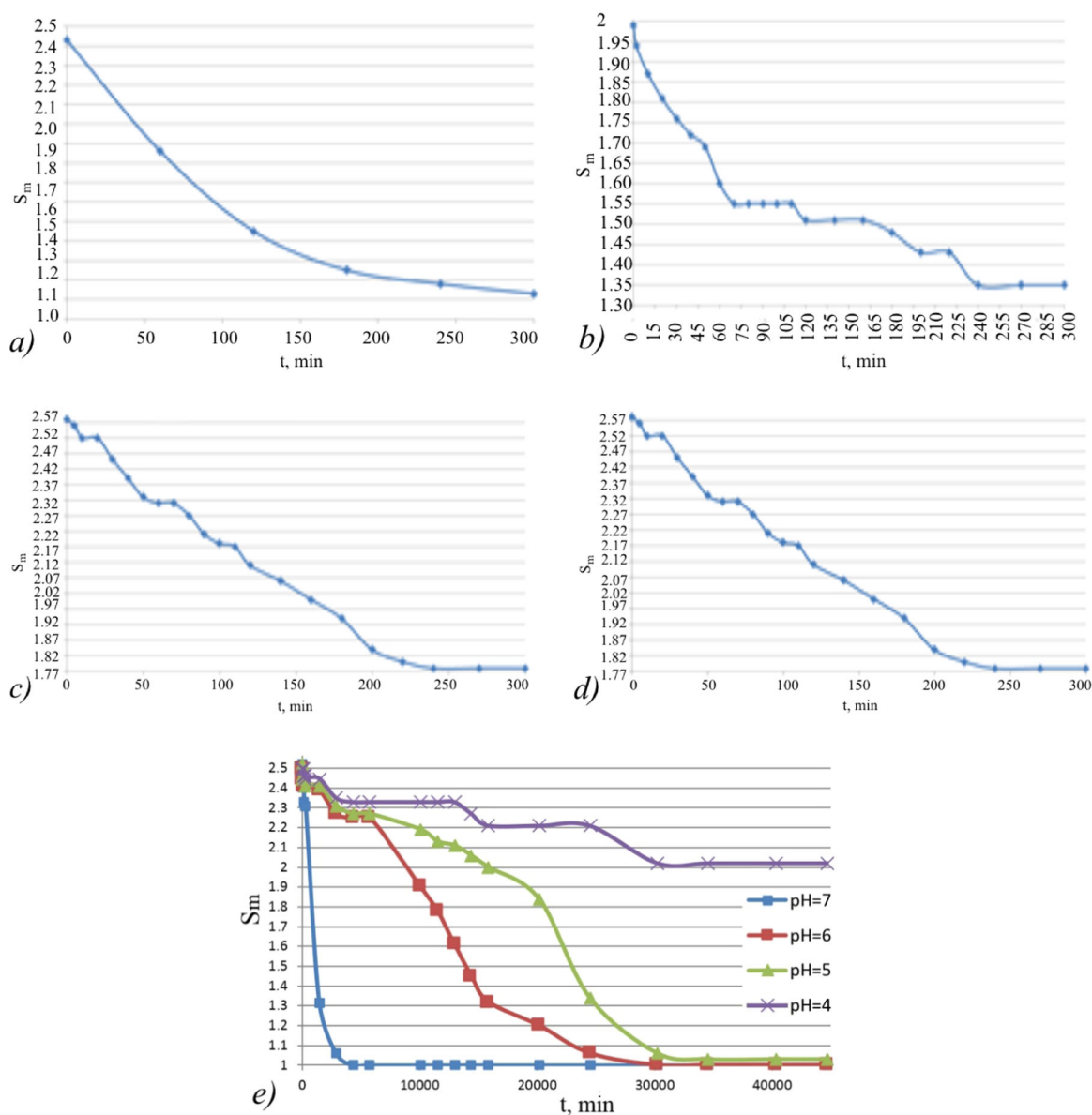


Fig. 1 OSA polycondensation data in a hydrothermal medium at different pH and temperatures. **a** 20 °C, pH = 8.47; **b** 50 °C, pH = 8.75; **c** 20 °C, pH = 8.7; **d** 20 °C, pH = 8; **e** 20 °C, pH = 7, 6, 5, 4

The initial concentration of C_s silicic acid corresponded to the solubility of amorphous silica at 100 °C. Then, the temperature of the solution was quickly lowered to 50 °C and the decrease in the concentration of C_s with time was determined at 50 °C, pH = 8.75, $C_e(50\text{ °C}) = 206.9\text{ mg/kg}$. The time τ_p at 50 °C was 4.0 h.

3.3 Kinetics of polycondensation at different pH

Figure 1c–e presents the results of a series of experiments to study the effect on the kinetics of polycondensation of the pH of an aqueous solution at 20 °C. Before starting measurements, water samples were heated at 96–98 °C to dissolve colloidal silica, and then quickly cooled to 20 °C and

acidified to a predetermined pH value. Time τ_p for different pH values: pH = 8.0— $\tau_p = 9.2\text{ h}$; pH = 7.0— $\tau_p = 14.2\text{ h}$; pH = 6.0— $\tau_p = 225\text{ h}$; pH = 6.0— $\tau_p = 225\text{ h}$; pH = 5— $\tau_p = 377.5\text{ h}$, pH = 4.0— $\tau_p = 3240\text{ h}$. A decrease in pH to 5.0–4.0 was lead to an almost complete inhibition of the polycondensation of OSA.

With a decrease in the polycondensation temperature and an increase in the initial supersaturation S_m , the nucleation rate I_N increased and, accordingly, the final average diameter d_m of SiO_2 nanoparticles decreased, the polycondensation of OSA passed faster (Eqs. (4–6)). At pH = 8.5–9.3 and temperatures of 65–90 °C, the d_m values were 59–90 nm, at 40–65 °C, $d_m = 40–60\text{ nm}$, and at 20–40 °C, $d_m = 5–40\text{ nm}$ (Fig. 2).

Fig. 2 Histograms of the distribution of sizes of silica nanoparticles in samples of sols obtained by dynamic light scattering. Temperature of OSA polycondensation was: **a** 25 °C, $d_m = 14$ nm; **b** 45 °C, $d_m = 47.4$ nm; **c** 75 °C, $d_m = 72.7$ nm

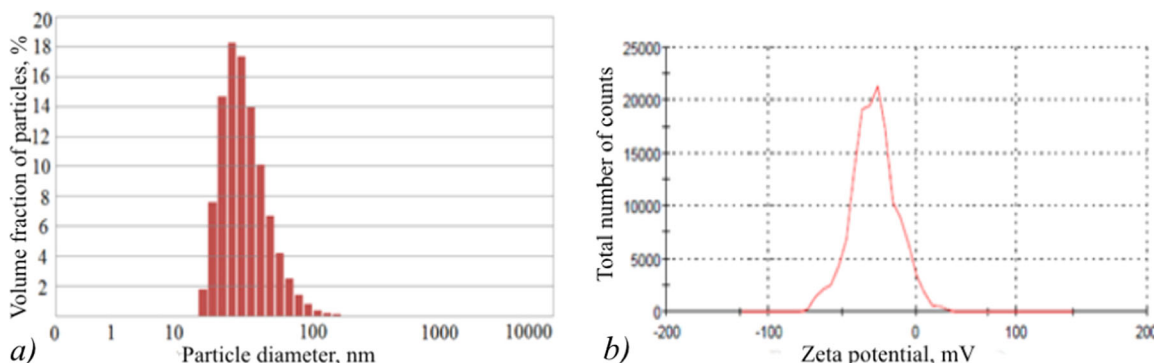
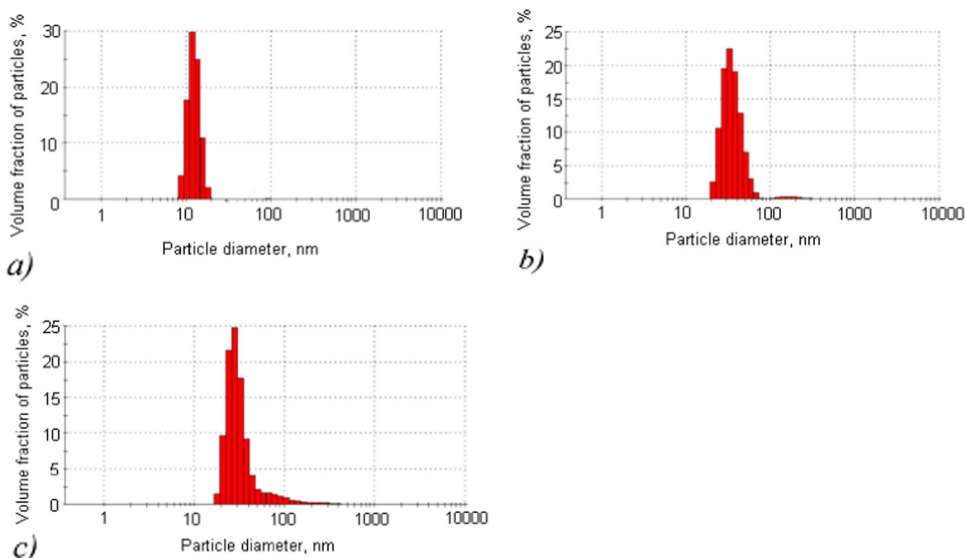


Fig. 3 Particle sizes and zeta potential of particles in a sol sample: **a** a histogram of the distribution of sizes of silica sol nanoparticles; **b** the zeta potential of the surface of sol nanoparticles

Table 3 The results of determining the average values of the diameter and zeta potential of the surface of the sol particles at various contents of SiO₂ in sols in the period 1–300 days after preparation

SiO ₂ , g/dm ³	The average particle diameter, nm				The average zeta potential, mV			
	1 day	60 days	210 days	300 days	1 day	60 days	210 days	300 days
82.5	27.0	27.0	31.0	31.0	-35.5	-30.1	-27.9	-29.7
28.1	52.0	52.0	46.0	52.0	-42.9	-39.8	-37.9	-41.3
22.5	62.0	60.0	50.0	58.0	-42.2	-39.3	-33.8	-33.7
16.4	70.0	60.0	63.0	55.2	-40.4	-40.2	-39.4	-39.8
13.2	60.0	60.0	67.0	65.3	-42.5	-39.4	-37.5	-38.9
10.9	42.0	43.0	43.0	39.0	-41.9	-32.6	-30.1	-27.9
6.15	57.0	64.0	69.0	66.0	-40.5	-39.3	-37.8	-38.8
3.28	45.0	42.0	40.0	51.0	-33.7	-30.7	-24.2	-27.2
2.06	85.0	85.0	78.0	77.0	-42.0	-39.6	-33.2	-36.5

4 Preparation of SiO₂ sols and their characteristics

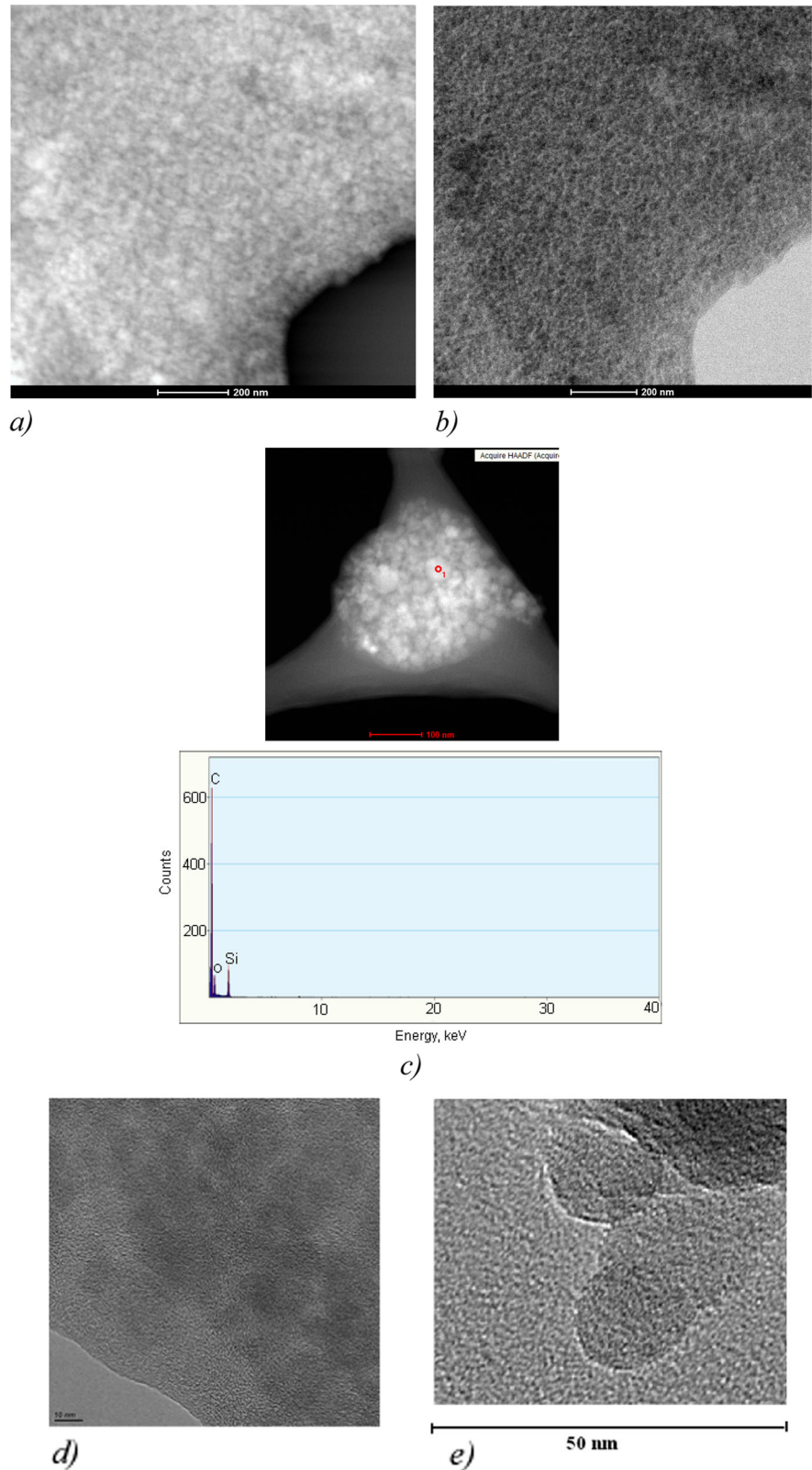
The size distribution of sol particles was determined by dynamic light scattering, and the particle zeta potential was determined by electrophoresis. Figure 3 shows the results of

determinations for one of the samples of the sol having the characteristics: density of the sol $\rho_s = 1080$ g/dm³, SiO₂ content = 150 g/dm³, pH = 8.6, average particle diameter of SiO₂ $d_m = 41.6$ nm, average value of zeta potential of the surface of SiO₂ particles $\xi_m = -28.2$ mV). The distribution curve of zeta potentials (Fig. 3b) was determined

by the combined method: comprehensive electrophoresis and dynamic light scattering, which allows one to take into

account the particle size and its effect on the particle velocity when an external electric field is applied.

Fig. 4 STEM HAADF, STEM BF, and TEM images of SiO_2 sol particles and EDX energy dispersive fluoroscopy. The content of SiO_2 is 178.7 g/dm^3 . **a** STEM HAADF image; **b** STEM BF image; **c** STEM HAADF image of particles and the results of EDX energy dispersive spectroscopy at selected point 1; **d** TEM image of particles; **e** TEM image of SiO_2 particle



The highest SiO₂ content in sols was 62.5 wt% ([SiO₂] = 940 g/dm³). Sols with SiO₂ content up to 62.5 wt% remained stable according to visual observations for at least 6 months. Table 3 shows the data on the control of changes in the average values of the diameter and zeta potential of the particle surface in sols within 300 days after preparation at various SiO₂ contents in the range from 2.06 to 82.5 g/dm³ (average diameters are determined by intensity of scattered light). In the period from 1 to 300 days, the average values of the diameter and zeta potential changed relatively insignificantly, without loss of particle stability, aggregation, flocculation, or gelation over 300 days.

Images of a fragment of SiO₂ sol particles obtained by scanning transmission spectroscopy in a dark field (Fig. 4a) and a bright field (Fig. 4b) showed the homogeneity of the amorphous structure of the material and the absence of ordered crystalline inclusions consisting of heavy elements with a large chemical element number *Z*. The energy dispersive fluoroscopy of the selected fragment (Fig. 4c) indicates that the elemental composition of the material is largely represented by Si and O, no impurities of other elements were detected. The spherical shape of SiO₂ particles, as well as their diameters and the absence of internal structures made up of atoms of heavy elements are shown by the image obtained by TEM (Fig. 4d, e).

At different SiO₂ contents in sols, the dependences of salinity and electrical conductivity were determined. Due to the use of ultrafiltration (parameter MWCO = 10–100 kD), the TDS content and the electrical conductivity of sols increased relatively weakly with increasing SiO₂ content. In this case, the dimensionless parameter $m_s = [\text{SiO}_2]/\text{TDS}$ with an increase in the SiO₂ content (mg/dm³) reached values of 300 or more (Table 3 and Fig. 5). Pores of ultrafiltration membrane on which a gel layer were accumulated caught SiO₂ nanoparticles. In this case, impurity ions passed through the gel layer and the pores of the membrane. SiO₂ nanoparticles

accumulated in the concentrate faster than cations and anions, especially up to the content of [SiO₂] = 200–240 g/dm³, respectively, the parameter m_s rapidly increased with [SiO₂] < 200–240 g/dm³, with [SiO₂] > 200–240 g/dm³, the growth rate m_s of the SiO₂ content decreased. The specific electrical conductivity of sols increased from 1.2 mS/cm at a content of [SiO₂] = 3 g/dm³ to 1.5 mS/cm at [SiO₂] = 475 g/dm³. This can be explained by the fact that as the thickness of the gel layer increases, the sorption capacity with respect to cations and anions increases. The inverse parameter $(1/m_s) = \text{TDS}/[\text{SiO}_2]$ continuously decreased with increasing [SiO₂] content in the sol. Thus, using ultrafiltration based on a hydrothermal solution, it is possible to obtain a concentrate with a high SiO₂ content and a low concentration of impurity ions—Na⁺, K⁺, Ca²⁺, Mg²⁺, Fe^{2.3+}, Al³⁺, SO₄²⁻, Cl⁻. Characteristics of sols are presented in Table 4.

5 SiO₂ gels and its characteristics

STEM HAADF, STEM BF, and TEM images of gel particles with a SiO₂ content of 10 wt% and the data of energy dispersive fluoroscopy are shown in Fig. 6. Images of SiO₂ gel particles show the uniformity and absence of ordered crystalline structures in fragments of the material and inside individual particles (Fig. 6a, b, d). The chemical composition of the material is represented by Si and O elements (Fig. 6c).

Figure 6 compares the rheological parameters of sols and gels. The sols are characterized by a linear dependence of the shear stress on the strain rate τ (G_p) (Fig. 7a). The values of the dynamic viscosity of sols, determined by the minimum of the dependence $\eta(G_p)$ in the Newtonian flow regime, for curves 3, 4, and 5, respectively, were $\eta = 1.69, 1.76, \text{ and } 1.86 \text{ MPa s}$ (20 °C) (Fig. 7b). For

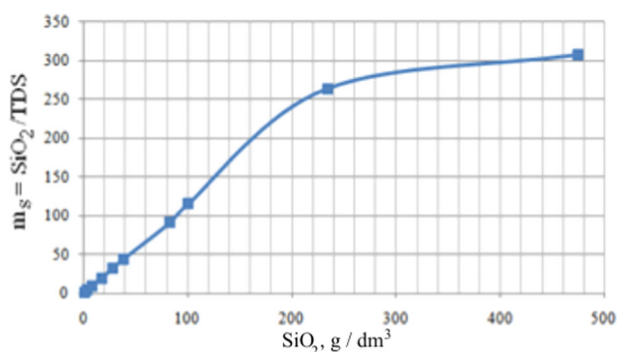
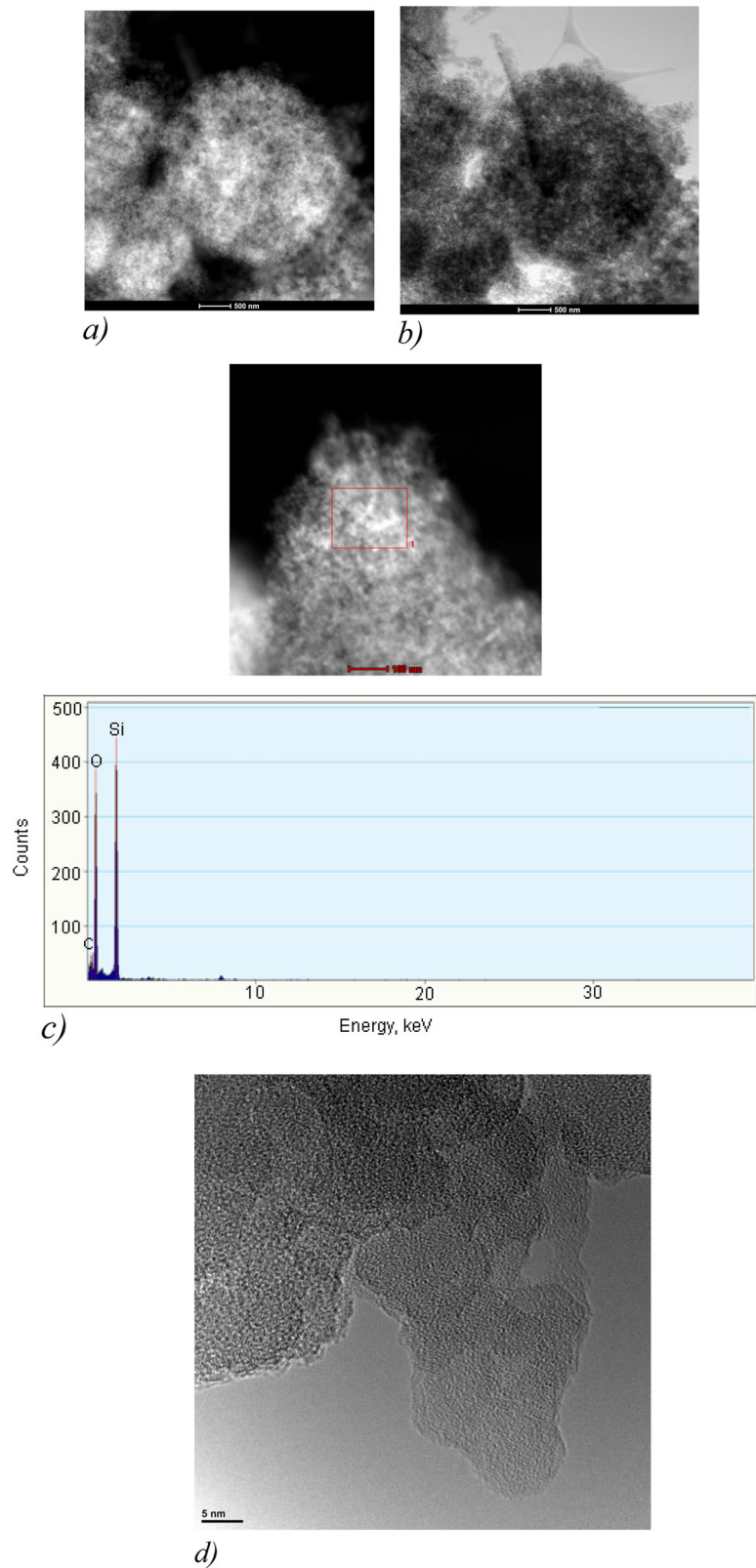


Fig. 5 Dependence of the parameter m_s on the SiO₂ content in silica sols

Table 4 Physical and chemical characteristics of water sols of silica obtained by ultrafiltration membrane concentration

Characteristics	Value
pH	8.0–9.2
Total content SiO ₂ , g/dm ³	3.0–940.0
Sol density ρ_s , g/dm ³	1000–1510
Average nanoparticle diameters d_m , nm	5–100
Salinity TDS, mg/dm ³	800–2000
Electrical conductivity σ_m , mS/cm (20 °C)	0.8–1.56
Average zeta potential ξ of nanoparticles surface, mV	–25.0 to –56.0
Dynamic viscosity η , mPa s (20 °C)	1.0–120.0
SiO ₂ content in solid phase precipitated from sol, wt%	Up to 99.72

Fig. 6 STEM HAADF, STEM BF, and TEM images of SiO₂ sol particles and EDX energy dispersive fluoroscopy. The SiO₂ content in the gel is 10 wt %; (a) STEM HAADF—image; (b) STEM BF—image; (c) STEM HAADF—image of particles and the results of energy dispersive spectroscopy EDX at selected point 1; (d) TEM image of particles



gels, the dependence of the shear stress τ on the strain rate G_p showed the yield strength of the order of 1000 and 10 Pa at a certain strain rate G_p (Fig. 7a). Above this the shear stress

ceased to change with increasing G_p , and the gel viscosity τ (G_p), accordingly, it began to decrease with increasing G_p (Fig. 7b). The gels showed the viscoplastic nature of the flow.

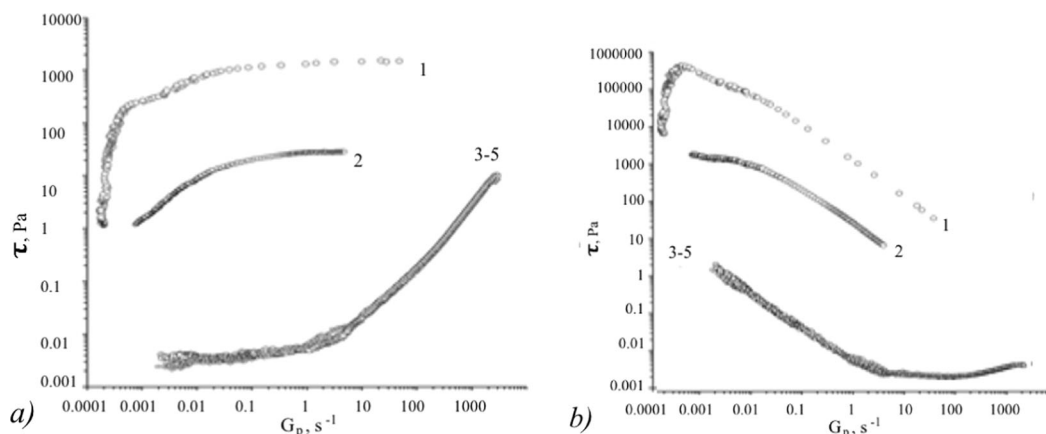


Fig. 7 Rheological characteristics: **a** the dependence of the shear stress τ on the strain rate G_p ; **b** the dependence of the dynamic viscosity η on the strain rate G_p . 1, 2—gels with SiO_2 content, respectively, 10 and 3.3 wt%; 3, 4, 5—sols with a SiO_2 content of 1.4, 2.8, and 3.3 wt%

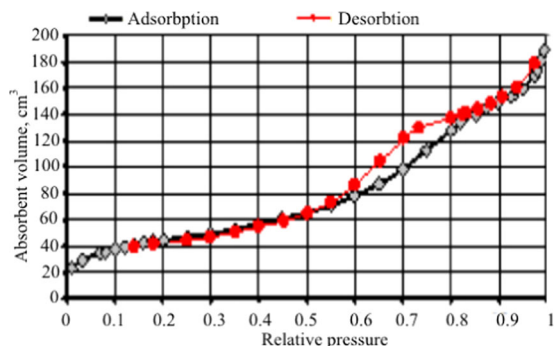


Fig. 8 Sorption–desorption curves for nanopowder obtained by vacuum sublimation

6 Preparation of mesoporous SiO_2 nanopowders

Cryogranules of sols and gels were subjected to vacuum sublimation to obtain powder samples. The UF-CVS-44 sample was obtained by cryochemical vacuum sublimation of a sol in which the SiO_2 content was increased by ultrafiltration membrane concentration to 40 g/dm³. Figure 8 shows the adsorption–desorption curve; Fig. 9 shows differential and integral distribution of the pores area and volume; Table 5 shows pore characteristics of the UF-CVS-44 sample (method of low-temperature nitrogen adsorption).

The spherical shape of the nanopowder particles obtained by cryochemical vacuum sublimation of a sol with a SiO_2 content of 22.5 g/dm³ was established by the SEM method with magnification factors from $\times 100,000$ to $\times 250,000$ (Fig. 10).

By reducing the temperature of the hydrothermal solution at the OSA polycondensation stage from 90 to 20 °C, it was achieved a decrease in the size of SiO_2 particles and, accordingly, an increase in their specific surface area and,

correspondingly, a decrease in the average pore diameter d_p :

$$d_p = 4 \cdot V_p / S_{\text{BET}} \quad (7)$$

With a decrease in temperature at the OSA polycondensation stage to 20 °C, the nanopowder BET-area increased to 500 m²/g, the pore volume was in the range 0.20–0.30 cm³/g, and the average pore size decreased to 2.0 nm.

When the content of $[\text{SiO}_2]$ in sols was from 2.4 to 90 g/dm³, the pour density of ρ_p powders after sublimation of water molecules from cryogranules and replacing them with air molecules was higher than the content of SiO_2 in sols and gels, i.e., SiO_2 nanoparticles compacted in volume after sublimation of water molecules (Table 6). So at $[\text{SiO}_2] = 2.4 \text{ g/dm}^3$, ρ_p was 20.5 g/dm³. When the content of $[\text{SiO}_2]$ in sols and gels was higher than 90 g/dm³ after the sublimation of water molecules, the SiO_2 nanoparticles were disaggregated in the volume with air molecules, and the powder density ρ_p became lower than the value of $[\text{SiO}_2]$: at $[\text{SiO}_2] = 520 \text{ g/dm}^3$, $\rho_p = 274 \text{ g/dm}^3$. In the range of $[\text{SiO}_2]$ contents in sols from 100 to 520 g/dm³, the ρ_p ($[\text{SiO}_2]$) dependence was close to linear.

Nanopowders samples had X-ray amorphous structure (Fig. 11). It was found [40] by comparison of thermogravimetric mass losses in the interval 200–1000 °C with Zhuravlev's constant that the density of surface silanol Si–OH groups in samples of hydrothermal nanopowders reaches 4.9 nm^{−2}, which provided its high chemical activity. The SiO_2 content in powders was raised up to 99.7 wt%.

Samples of SiO_2 nanopowder with specific surface area $S_{\text{BET}} = 410 \text{ m}^2/\text{g}$ were compacted on a hydraulic press at pressures of 1000–2000 MPa for 2 h, then, after hardening, they were calcined at a temperature of 1000 °C for 2 h. After compaction and calcination, the compressive strength of solid samples was determined using a Shimadzu instrument complex with registration of the stress–strain curves (Fig. 12). The compressive strength reached 337 MPa. This

Fig. 9 Characteristics of pores of UF-CVS-44 powder: **a** an integral curve of the distribution of area over pore diameters; **b** integral curve of the distribution of volume over pore diameters; **c** differential curve of the distribution of area by pore diameters; **d** differential curve of the distribution of volume over pore diameters

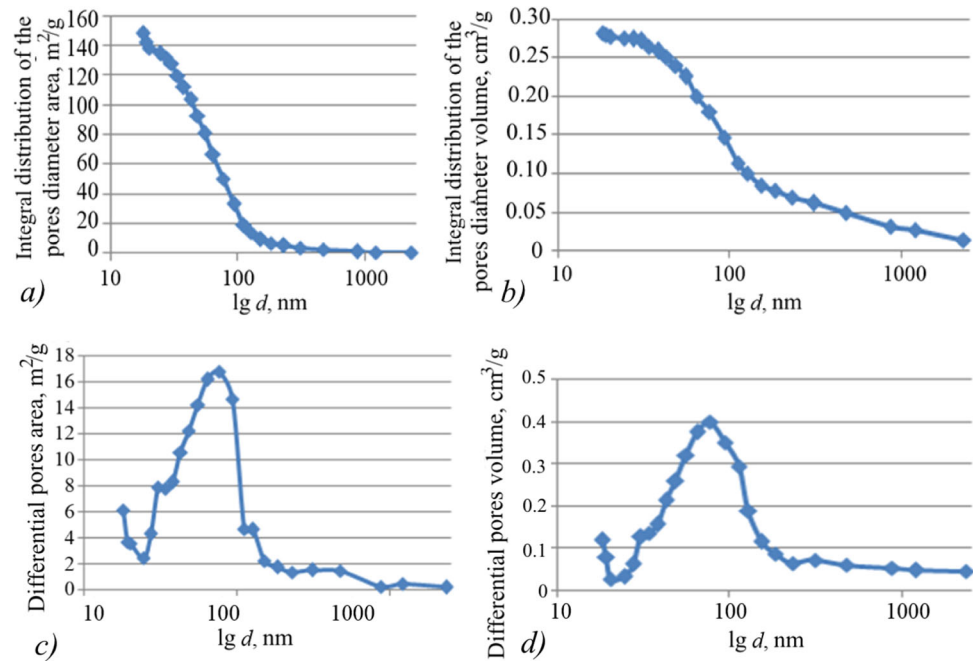


Table 5 Characteristics of pores of UF-CVS-44 powder

Characteristics	Unit of measurement	Value
S_{BET} area	m^2/g	165
Pore volume, determined by single point, V_p	cm^3/g	0.25
Average pore diameter, d_p	nm	6.0
Average pore diameter by the adsorption curve	nm	7.6
Average pore diameter by the desorption curve	nm	7.1
Micropore area	m^2/g	6.5
Micropore volume	cm^3/g	0.0005

indicates a high specific surface and density of the surface silanol groups of SiO_2 nanopowders. Sizes of the sample—(thickness \times width \times height), mm: $5.0 \times 11.9 \times 2.9$; sample density— 1.7 g/cm^3 ; indentation speed— 1 mm/min ; maximum force— 20057.6 N ; maximum stress— 337.1 N/mm^2 ; stroke amplitude— 1.681 mm ; maximum elongation— 1.681 mm ; maximum deformation— 57.88% ; maximum time— 100.95 s .

7 Prospects for research and applications of hydrothermal nanosilica

The obvious continuation of the work is follows research:

- (1) Processes of formation of thin films by sol–gel transition;

- (2) formation of glasses;
- (3) formation of ceramic forms based on sols and nanopowders;
- (4) receiving airgels;
- (5) receiving heat insulators;
- (6) obtaining noble opal matrices by manipulating the parameters T , pH , I_N , R_{md} and reconstructing the conditions for the existence of hydrothermal nanocolloids [41];
- (7) optical properties of sols with a surface modified by metal nanoparticles [42];
- (8) rheological properties of sols and gels at different ages,
- (9) sorption capacity of mesoporous nanopowders.

Using SiO_2 nanoparticles of sols and nanopowders having a high and chemically active surface, it is possible to purposefully influence to [43–47]:

- (1) Kinetics of hydration of the main cement minerals C_3S , C_2S , C_3A , C_4AF ;
- (2) reducing the size and shape of the particles of the gel of the hydrates of calcium silicate C–H–S, increasing the density of their packaging;
- (3) increase the volume fraction of C–H–S gel with greater elasticity and hardness, and, as a result, increase the compressive and bending strength of concrete, reduce pore volume, increase frost resistance, chemical resistance, and, as a result, the durability of concrete.

A sufficiently developed application of hydrothermal nanoparticles of sols and SiO_2 powders is the intensification

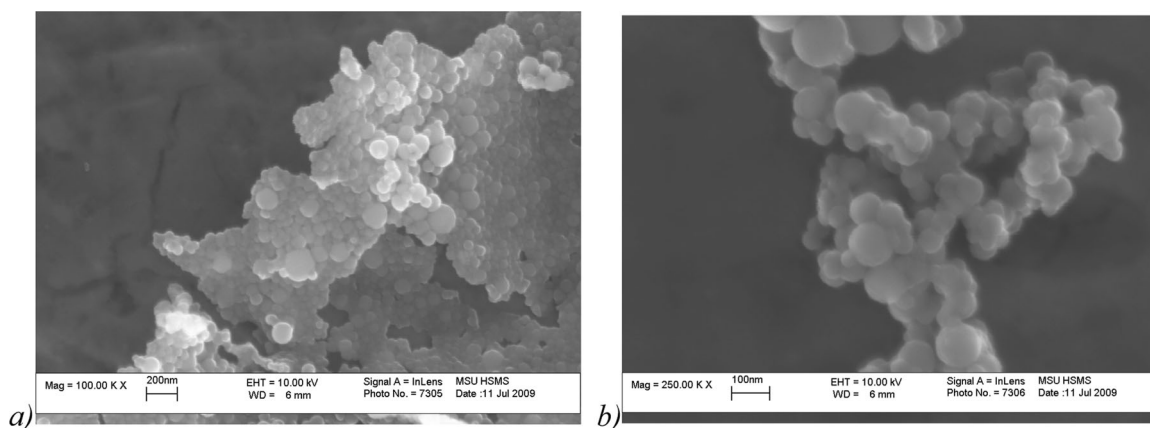


Fig. 10 SEM images of silica powder nanoparticles (**a**) $\times 100,000$; (**b**) $\times 250,000$ times

Table 6 Pour density of nanopowders ρ_p depending on the SiO_2 content in the sol

$[\text{SiO}_2]$, g/dm ³	2.4	5.2	6.93	10.4	17.56	32	65.85	120	131.7	160	260	520
ρ_p , g/dm ³	20.5	29	35	43.8	55	55	84	91	100	117	168	274

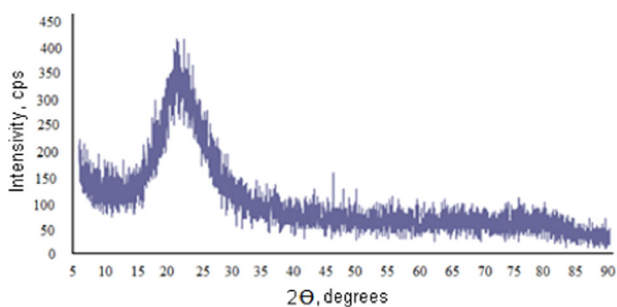


Fig. 11 X-Ray diffraction data of amorphous silica nanopowder. (CuK α wave length $\lambda = 1.54 \text{ \AA}$)

of photosynthesis in plant cell chloroplasts due to the photoluminescent radiation of SiO_2 nanoparticles, an increase in the proportion of photosynthetic pigments of chlorophylls *a* and *b*. As a result, an increase in the growth rate, biochemical and biometric indicators at all stages of plant growth and development, a significant increase in the yield of agricultural plants [48]. Hydrothermal nanosilica is used as a feed additive that increases the productivity of farm animals [49].

Nontoxic sols, gels, and mesoporous nanopowders can be the basis for the creation of medicines:

- (1) Enterosorbents;
- (2) Carrier nanoparticles for targeted delivery of drugs fixed on the surface of nanoparticles to cells of various body tissues or capsule shells containing medicinal substances inside [50];

- (3) Drugs that improve the strength and plasticity of the articular-bone tissue.

8 Conclusion

- (1) It is shown that, based on a hydrothermal solution, it is possible to obtain nanosized forms of SiO_2 —sols, gels, and powders. To achieve this, the use of OSA polycondensation at certain pH and temperature, ultrafiltration membrane concentration, sol–gel transition, and cryochemical vacuum sublimation is required.
- (2) With decreasing temperature and increasing supersaturation of the hydrothermal medium S_m , the nucleation rate of I_N increases, the duration of the process of polycondensation of OSA and the growth of SiO_2 nanoparticles decreases, and the final average nanoparticle diameter d_m decreases. A decrease in the pH of the hydrothermal medium reduces the I_N rate, increases the final diameter d_m of the nanoparticles, and leads to an increase in the duration of OSA polycondensation.
- (3) The choice of pore sizes of polymer ultrafiltration membranes (parameter MWCO 10–100 kD) can provide high selectivity for SiO_2 nanoparticles and low selectivity for ions of dissolved salts. The value of the zeta potential of the surface of nanoparticles in concentrated sols falls within the range from -56 to -25 mV, which ensures particle stability to aggregation

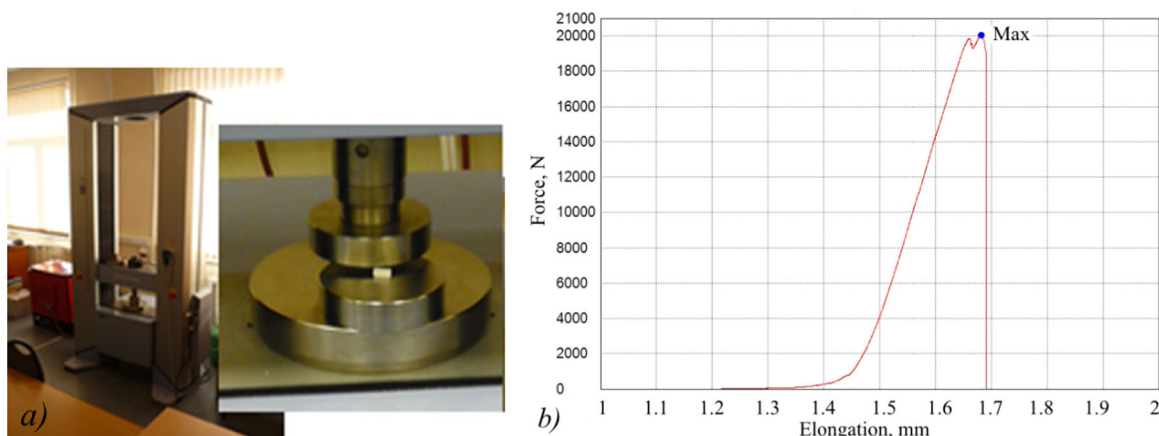


Fig. 12 Compression strength test results for a compacted SiO₂ nanopowder. **a** The appearance of a compacted SiO₂ nanopowder obtained by vacuum sublimation of a gel; **b** the force–elongation curve when testing a compacted sample for compressive strength

due to electrostatic repulsion and stability of sols with SiO₂ content in sol up to 62.5 wt%.

- (4) By varying the temperature at the polycondensation stage from 20 to 90 °C at pH = 8.5–9.3, one can adjust the final mean particle diameter of SiO₂ in the range from 5 to 100 nm, respectively, the specific surface area of the particles from 50 to 500 m²/g. The mean mesopore diameter of SiO₂ powders, due to the specific surface area of the particles, is regulated within 2–15 nm. Bulk density of nanopowders depends on SiO₂ content in sols.
- (5) By lowering the pH of sols to 5–6, gels with rheological characteristics depending on the SiO₂ content can be obtained. The dependences of shear stress and dynamic viscosity on shear rate showed the viscoplastic nature of the flow of gels, in contrast to the Newtonian flow of sols.
- (6) The physical and chemical characteristics of hydrothermal nanosilica allow it to be used to produce various materials: thin films, glass, ceramics, concrete nanomodifiers, plant growth accelerators, and medications.

Compliance with ethical standards

Conflict of interest The authors declare that they have no conflict of interest.

Publisher's note Springer Nature remains neutral with regard to jurisdictional claims in published maps and institutional affiliations.

References

1. Hanaor DAH, Chironi I, Karatchevtseva I et al. (2012) Single and mixed phase TiO₂ powders prepared by excess hydrolysis of titanium alkoxide. *Adv Appl Ceram.* <https://doi.org/10.1179/1743676111Y.0000000059>
2. Danks AE, Hall SR, Schnepf Z (2016) The evolution of “sol-gel” chemistry as a technique for materials synthesis. *Mater Horizons.* <https://doi.org/10.1039/c5mh00260e>
3. Liu P, Heinson WR, Sorensen CM, Chakrabarty RK (2019) Kinetics of sol-to-gel transition in irreversible particulate systems. *J Colloid Interface Sci.* <https://doi.org/10.1016/j.jcis.2019.04.067>
4. Yang H, Zhao D (2005) Synthesis of replica mesostructures by the nanocasting strategy. *J Mater Chem* 15:1217–1231. <https://doi.org/10.1039/B414402C>
5. Akkerman QA, Rainò G, Kovalenko MV, Manna L (2018) Genesis, challenges and opportunities for colloidal lead halide perovskite nanocrystals. *Nat Mater.* <https://doi.org/10.1038/s41563-018-0018-4>
6. Kongsong P, Sikong L, Niyomwas S, Rachpech V (2014) Photocatalytic antibacterial performance of glass fibers thin film coated with N-doped SnO₂/TiO₂. *Sci World J.* <https://doi.org/10.1155/2014/869706>
7. Ruckdeschel P, Kemnitzer TW, Nutz FA, et al. (2015) Hollow silica sphere colloidal crystals: insights into calcination dependent thermal transport. *Nanoscale.* <https://doi.org/10.1039/c5nr00435g>
8. Wan Y, Zhao D (2007) On the controllable soft-templating approach to mesoporous silicates. *Chem Rev.* 107:2821–2860
9. Moreno R (2012) Colloidal processing of ceramics and composites. *Adv Appl Ceram.* <https://doi.org/10.1179/1743676111Y.0000000075>
10. Yakovlev AV, Milichko VA, Vinogradov VV, Vinogradov AV (2016) Inkjet color printing by interference nanostructures. *ACS Nano.* <https://doi.org/10.1021/acsnano.5b06074>
11. Yakovlev AV, Milichko VA, Vinogradov VV, Vinogradov AV (2015) Sol-gel assisted inkjet hologram patterning. *Adv Funct Mater.* <https://doi.org/10.1002/adfm.201503483>
12. Wang SF, Zhang J, Luo DW et al. (2013) Transparent ceramics: processing, materials and applications. *Prog Solid State Chem.* 41:20–54
13. Yoldas BE (1979) Monolithic glass formation by chemical polymerization. *J Mater Sci.* <https://doi.org/10.1007/BF00551023>
14. Zhang G, Wang Y, Fu Z et al. (2009) Transparent mullite ceramic from single-phase gel by Spark Plasma Sintering. *J Eur Ceram Soc.* <https://doi.org/10.1016/j.jeurceramsoc.2009.04.012>
15. Volodina KV, Solov'eva NL, Vinogradov VV, et al. (2014) A synergistic biocomposite for wound healing and decreasing scar size based on sol-gel alumina. *RSC Adv.* <https://doi.org/10.1039/c4ra09015b>

16. Giesche H (1994) Synthesis of monodispersed silica powders II. Controlled growth reaction and continuous production process. *J Eur Ceram Soc.* [https://doi.org/10.1016/0955-2219\(94\)90088-4](https://doi.org/10.1016/0955-2219(94)90088-4)
17. Wang HC, Wu CY, Chung CC et al. (2006) Analysis of parameters and interaction between parameters in preparation of uniform silicon dioxide nanoparticles using response surface methodology. *Ind Eng Chem Res.* <https://doi.org/10.1021/ie060299f>
18. Bredereck K, Effenberger F, Tretter M (2011) Preparation and characterization of silica aquasols. *J Colloid Interface Sci.* <https://doi.org/10.1016/j.jcis.2011.04.062>
19. Wu SH, Lin HP (2013) Synthesis of mesoporous silica nanoparticles. *Chem Soc Rev.* <https://doi.org/10.1039/c3cs35405a>
20. Innocenzi P, Martucci A, Guglielmi M et al. (2001) Mesoporous silica thin films for alcohol sensors. *J Eur Ceram Soc.* [https://doi.org/10.1016/S0955-2219\(01\)00156-X](https://doi.org/10.1016/S0955-2219(01)00156-X)
21. Paul J, Romeis S, Mačković M et al. (2015) In situ cracking of silica beads in the SEM and TEM—effect of particle size on structure-property correlations. *Powder Technol.* <https://doi.org/10.1016/j.powtec.2014.10.026>
22. Bagheri E, Ansari L, Abnous K et al. (2018) Silica based hybrid materials for drug delivery and bioimaging. *J. Control. Release*
23. Jang J, Yoon H (2004) Novel fabrication of size-tunable silica nanotubes using a reverse-microemulsion-mediated sol-gel method. *Adv Mater.* <https://doi.org/10.1002/adma.200306567>
24. Loganina VI, Kislitsyna SN, Mazhitov YB (2018) Development of sol-silicate composition for decoration of building walls. *Case Stud Constr Mater.* <https://doi.org/10.1016/j.cscm.2018.e00173>
25. Deng Z, Chen M, Zhou S et al. (2006) A novel method for the fabrication of monodisperse hollow silica spheres. *Langmuir.* <https://doi.org/10.1021/la060944n>
26. Kao KC, Lin CH, Chen TY et al. (2015) A general method for growing large area mesoporous silica thin films on flat substrates with perpendicular nanochannels. *J Am Chem Soc.* <https://doi.org/10.1021/jacs.5b01180>
27. Checmanowski JG, Szczygieł I, Mazur A, Szczygieł B (2019) Protective properties of SiO₂ with SiO₂ and Al₂O₃ nanoparticles sol-gel coatings deposited on FeCrAl alloys. *Ceram Int.* <https://doi.org/10.1016/j.ceramint.2018.07.295>
28. Matysiak W, Tański T (2019) Analysis of the morphology, structure and optical properties of 1D SiO₂ nanostructures obtained with sol-gel and electrospinning methods. *Appl Surf Sci.* <https://doi.org/10.1016/j.apsusc.2019.05.090>
29. Liu Y, Cai Z, Sheng L et al. (2019) Influence of nanosilica on inner structure and performance of chitosan based films. *Carbohydr Polym.* <https://doi.org/10.1016/j.carbpol.2019.02.079>
30. Sowntharya L, Gundakaram RC, Soma Raju KRC, Subasri R (2013) Effect of addition of surface modified nanosilica into silica-zirconia hybrid sol-gel matrix. *Ceram Int.* <https://doi.org/10.1016/j.ceramint.2012.10.276>
31. Cai Y, Li X, Dong J (2014) Microstructure and mechanical properties of porous Si₃N₄-SiO₂ ceramics fabricated by a process combining carbothermal reduction and sol-gel infiltration-sintering. *Mater Sci Eng A.* <https://doi.org/10.1016/j.msea.2014.01.087>
32. Pronin IA, Goryacheva MV (2013) Principles of structure formation and synthesis models produced by the sol-gel method SiO₂-Me_xO_y nanocomposites. *Surf Coatings Technol.* <https://doi.org/10.1016/j.surfcoat.2013.09.009>
33. Asadi Z, Norouzbegi R (2018) Synthesis of colloidal nanosilica from waste glass powder as a low cost precursor. *Ceram Int.* <https://doi.org/10.1016/j.ceramint.2018.09.050>
34. Crerar DA, Anderson GM (1971) Solubility and solvation reactions of quartz in dilute hydrothermal solutions. *Chem Geol.* [https://doi.org/10.1016/0009-2541\(71\)90052-0](https://doi.org/10.1016/0009-2541(71)90052-0)
35. Marshall WL, Warakomski JM (1980) Amorphous silica solubilities-II. Effect of aqueous salt solutions at 25 °C. *Geochim Cosmochim Acta.* [https://doi.org/10.1016/0016-7037\(80\)90281-1](https://doi.org/10.1016/0016-7037(80)90281-1)
36. Rothbaum HP, Rohde AG (1979) Kinetics of silica polymerization and deposition from dilute solutions between 5 and 180 °C. *J Colloid Interface Sci.* [https://doi.org/10.1016/0021-9797\(79\)90328-X](https://doi.org/10.1016/0021-9797(79)90328-X)
37. Iler RK (1979) The chemistry of silica: solubility, polymerization, colloid and surface properties, and biochemistry. *Lavoisierfr.* <https://doi.org/10.1002/ange.19800920433>
38. Weres O, Yee A, Tsao L (1981) Kinetics of silica polymerization. *J Colloid Interface Sci.* [https://doi.org/10.1016/0021-9797\(81\)90230-7](https://doi.org/10.1016/0021-9797(81)90230-7)
39. Potapov VV, Cerdan AA, Kashutina IA (2019) Numerical simulation of orthosilicic acid polycondensation and silica particles formation in hydrothermal solutions. *Volcanol seismol.* <https://doi.org/10.31857/s0203-03062019418-28>
40. Potapov VV, Zhuravlev LT (2005) Temperature dependence of the concentration of silanol groups in silica precipitated from a hydrothermal solution. *Glas Phys Chem.* <https://doi.org/10.1007/s10720-005-0111-z>
41. Potapov VV, Kamashev DV (2006) Synthesis of precious opal in a hydrothermal solution. *Glas Phys Chem.* <https://doi.org/10.1134/S1087659606010123>
42. Potapov VV, Revina AA, Baranova EK (2008) The optical properties of nanodisperse silica in hydrothermal solutions. *Russ J Phys Chem A.* <https://doi.org/10.1134/S0036024408060253>
43. Sobolev K, Gutiérrez MF (2005) How nanotechnology can change the concrete world. *Am Ceram Soc Bull.* <https://doi.org/10.1002/9780470588260.ch17>
44. Sanchez F, Sobolev K (2010) Nanotechnology in concrete—a review. *Constr Build Mater.* 24:2060–2071
45. Flores-Vivian I, Pradoto RGK, Moini M, et al. (2017) The effect of SiO₂ nanoparticles derived from hydrothermal solutions on the performance of portland cement based materials. *Front Struct Civ Eng.* <https://doi.org/10.1007/s11709-017-0438-2>
46. Potapov VV, Efimenko YV, Gorev DS (2019) Modification of concrete by hydrothermal nanosilica. *Nanotechnologies in Construction.* 11:248–265. <https://doi.org/10.15828/2075-8545-2019-11-3-248-265>
47. Lapin AA, Kalayda ML, Potapov VV et al. (2018) The influence of hydrothermal nanosilica powder aquasuspensions on the vital capacity of *Daphnia magna* Straus crustaceans. *Int J nanotechnol* 15:422–432
48. Zelenkov VN, Ivanova MI, Potapov VV (2019) Hydrothermal nanosilica in the agrotechnology of radish cultivated in the conditions of low positive temperature. *AIP Conf Proc* 2063:040069. <https://doi.org/10.1063/1.5087401>
49. Fediuk R, Mochalov A, Timokhin R (2018) Review of methods for activation of binder and concrete mixes. *AIMS Mater Sci* 5. <https://doi.org/10.3934/matserci.2018.5.916>
50. Palamarchuk KV, Artemov VV, Bukreeva TV (2018) Microcapsules based on pickering emulsion and polyelectrolyte layers: biomedical applications. *Nanotechnol Russ.* <https://doi.org/10.1134/S1995078018020076>